Perylene diimide nanoprobes for in vivo tracking of mesenchymal stromal cells using photoacoustic imaging

Yonghong Yang,[†,‡] Claudia Fryer,[†,‡] Jack Sharkey,[‡] Aidan Thomas,[†] Ulrike Wais,[†,‖] Alexander W. Jackson,[‖] Bettina Wilm,[‡] Patricia Murray,[‡] and Haifei Zhang[†]*

[†] Department of Chemistry, University of Liverpool, Oxford Street, Liverpool, L69 7ZD, UK.

[‡] Department of Cellular and Molecular Physiology, Institute of Translational Medicine, University of Liverpool, Crown Street, Liverpool, L69 3BX, UK.

[‖] Institute of Chemical and Engineering Science, 1 Pesek Road, Jurong Island 627833, Singapore.

KEYWORDS: perylene diimide, photoacoustic imaging, organic nanoparticles, in vivo tracking, star hyperbranched polymer.

ABSTRACT. Non-invasive bioimaging techniques are critical for assessing the biodistribution of cellular therapies longitudinally. Among them, photoacoustic imaging (PAI) can generate high resolution images with tissue penetration depth of ~ 4 cm. However, it is essential and still highly challenging to develop stable and efficient near infra-red (NIR) probes with low toxicity for PAI. We report here the preparation and use of perylene diimide derivative (PDI) with NIR absorbance (around 700 nm) as nanoprobes for tracking mesenchymal stromal cells (MSCs) in mice. Employing an in-house synthesized star hyperbranched polymer as stabilizer is the key to the formation of stable PDI nanoparticles with low toxicity and high uptake by the MSCs. The PDI nanoparticles remain within the MSCs as demonstrated by *in vitro* and *in vivo* assessments. The PDI-labelled MSCs injected subcutaneously on the flanks of the mice are clearly visualized with PAI up to 11 days post-administration. Furthermore, bioluminescence imaging of PDI-labelled luciferase-expressing MSCs confirms that the administered cells remain viable for the duration of the experiment. These PDI nanoprobes thus have good potential for tracking administered cells *in vivo* using PAI.

1. INTRODUCTION

Cell-based regenerative medicine therapies (RMTs) are being explored as treatments for the diseases of different types. Mesenchymal stromal cells (MSCs) have been the most widely used RMT, but despite showing therapeutic effects in a range of animal disease models, the results of most clinical trials have so far been disappointing.[1-4] Due to the challenges of monitoring the fate of administered cells, it is not clear if this lack of efficacy in the clinic is due to the cells not reaching their target, or their failure to persist in the target organ. A further problem with cell-based RMTs is the risk of tumourigenicity.[5-7] Strategies that assess the growth, function, and biodistribution of administered cells longitudinally *in vivo* would allow better understanding of their behavior and mechanisms of action, potentially facilitating the development of safer and more efficacious treatments.[5,7]

A number of non-invasive techniques have been employed to monitor cells *in vivo*, but all have some limitations.[5,8] For instance, magnetic resonance imaging (MRI) can generate images with good spatial resolution but low temporal resolution, making it difficult to perform whole body scans. Fluorescence imaging (FI) has good temporal resolution but poor sensitivity, making it difficult to detect small numbers of cells. Bioluminescence imaging (BLI) has much greater sensitivity but poor spatial resolution, making it difficult to determine the precise location of the cells.[5] Photoacoustic imaging (PAI) is a technique that can potentially address the shortcomings of the imaging methods mentioned above.[9] This is because PAI exhibits high sensitivity, can image small numbers of cells in high tissue depth, and generate images of good spatial and temporal resolution. This makes it possible do whole body imaging of small cells.[5,9] Near infrared (NIR) light is used in PAI to illuminate tissue and detect generated ultrasound wave (which have much lower scattering tendency by biological media and tissue than photons).[8,10] This allows the

visualisation of targeted tissues and sub-organ structures at several centimeters of depth. With PAI, it is possible to image the entire depth of a mouse or tissues close to skin surface for large animals and human being. In general, PAI instruments operate as follows: when tissue is illuminated with NIR light, photo-absorbers present within the tissue absorb the light and undergo thermoelastic expansion, generating acoustic waves that can be detected at the body surface.[9,10] Multispectral Optoacoustic Tomography (MSOT) is one type of PAI. MSOT utilizes multiple excitation wavelengths and allows multiple photo-absorbers to be identified simultaneously.[11,12] Thus, MSOT is capable of imaging at multiple wavelengths and the information obtained from multiple wavelengths improves image accuracy. Each of the multiple photo-absorbers can be identified by spectrally unmixing, providing detailed information about the imaged subject.[11-13]

Endogenous chromophores and exogenous contrast agents have been used as photo-absorbers for PAI.[10, 14-15] These chromophores are good probes for PAI because they absorb light within the NIR region (approximately NIR-I window for 700 – 1000 nm and NIR-II window for 1000 – 1700 nm) which shows less tissue absorption & photon scattering and lower levels of autofluorescence.[10, 15-17] Endogenous chromophores include haemoglobin, lipid, and melanin, and genetically engineering chromophores or reporter genes (which can be expressed *in situ* over a long period, and is highly useful for longitudinal studies).[10,14] Exogenous contrast agents are employed to improve PAI image contrast for various targeted applications. Exogenous PA contrast agents can be divided into molecules (mainly organic dyes including cyanine dyes, phthalein and xanthene dyes, squaraine and coroconaine dyes, *etc.)*[18] and nanostructured materials.[16, 19-20] Many types of nanostructure materials have been fabricated and investigated for PAI, which may be classified into inorganic materials (including metal (mostly gold) nanoparticles,[17] semiconducting nanomaterials, carbon nanostructures, quantum dots), organic nanomaterials (including

semiconducting and conjugated polymer nanoparticles),[21-24] and hybrid nanocomposites.[10,16,20] While inorganic materials as PAI nanoprobes are highly stable and produce bright images, organic nanoprobes can offer reduced toxicity (e.g., no heavy metals) and the flexibility in material functionality and light absorbance wavelength via chemical synthesis.[21-24]

Perylene diimide (PDI) derivatives are one type of small molecule dyes which are extensively used in pigment and optoelectronics industries.[25-26] They can be readily modified at the bay positions or by core expansion to induce fluorescence and NIR absorption with high quantum yield and high photostability.[27-29] Furthermore, the solubility of PDIs in different solvents can be achieved by modifying groups at the imide positions and/or inducing bulky substitutes to the bay positions.[29-30] Due to their design and synthetic potential, both hydrophobic and water-soluble PDIs with NIR absorbance have been used for PAI and photothermal treatment of cancer cells.[31] Examples include the use of hydrophobic PDI nanoparticles,[32] ^{64}Cu-labeled amphiphilic PDI nanoparticles,[33] zwitterionic PDI nanoparticles,[34] and self-assembled terrylenediimide (TDI)-based & quaterrylenediimides (QDI) nanoparticles.[35,36]

In spite of the exciting use of NIR-absorbing PDI for PAI and photothermal treatment of cancer cells, as far as we are aware, the use of PDI nanoparticles for cell labelling has not been reported. Cell tracking, which follows specific cells in vivo and aims to determine cell location, fate, functionality or differentiation, is critical for optimizing cellular therapies including stem-cell treatment as well as adoptive immunotherapy.[37,38] Various non-invasive imaging techniques, for example, MRI, FLI, BLI, positron emission tomography (PET), have played key roles in cell tracking.[37-39] Due to its potential in producing high resolution images with high tissue depth, PAI has begun to be used as a promising technique for cell tracking.[39-43] Gold nanostructures have

been the main contrast agents for use in tracking cells by PA[40,41,43] whilst semiconducting polymer nanoparticles were also used in labelling and tracking stem cells.[42]

In this study, the potential of PDIs with NIR-absorbing properties was investigated as imaging probes to enable cell tracking with MSOT. As previously demonstrated,[27-36] PDI nanoparticles are photostable, have a high extinction coefficient, feasibility of varying absorbance wavelength by changing synthesis conditions, and do not comprise heavy metals. PDIs, in the form of self-assembled structures or nanoparticles, have been used as photoacoustic probes in various fields. However, PDI nanoparticles can be highly effective for in vivo cell tracking, due to their unique photostability and high sensitivity/intensity over a longer imaging period. Herein, hydrophobic PDI nanoparticles were prepared in aqueous medium by a nanoprecipitation approach with the use of in-house synthesized star hyperbranched polymer (SHBP) as the biocompatible polymeric surfactant.[44] We demonstrated that these PDI nanoparticles could label mouse MSCs and enable them to be tracked *in vivo* for 11 days with MSOT following subcutaneous injection in mice. Moreover, by using a bimodal MSOT-BLI strategy, we confirmed that the PDI-labelled MSCs remained viable following *in vivo* administration.

2. EXPERIMENTAL SECTION

2.1. Materials. All chemicals and solvents were bought from Sigma Aldrich or Fisher and used as received. The star hyperbranched polymer (SHBP) (DEAEMA$_{50}$-*c*-DEGDMA$_2$)-*b*-(OEGMA$_{80}$) was synthesized in the group (see Supporting Information).[44]

2.2. Synthesis of PDI nanoparticles. Perylenetetracarboxylic dianhydride (PTCDA) was used as the starting material. Brominated PTCDA was firstly synthesized (Scheme S1), following

a previously report method with modifications.[45] Brominated PTCDA was then used to synthesize the NIR-active PDI.[46] All the PDIs were purified by column purification and recrystallization (see Supporting Information).

PDI solution in acetone (1 mg/ml) was firstly prepared. A second solution was then prepared with PVA or the SHBP ($DEAEMA_{50}$-*c*-$DEGDMA_2$)-*b*-($OEGMA_{80}$) in acetone (2 mg/ml). These solutions were combined to achieve PDI:SHBP ratios of 1:1, 1:2 and 2:1 and made up to a volume of 2 ml with acetone. The acetone solution was then added to water (8 ml) in a dropwise manner while the water phase was stirred. The solution was stirred for 24 hours to allow the acetone to evaporate, yielding a clear, green aqueous nanoparticle suspension. No observation of large particles and colourless & transparent liquid phase after centrifuging with speed of 13,000 rpm indicated high yield of PDI nanoparticle formation. It should be pointed out that the observation was only qualitative. The calculation of encapsulation efficiency and loading content could be performed via the quantification of PDI in the nanoparticles by dissolving the PDI nanoparticles in acetone and subsequent UV-Vis absorption analysis.

^1H and ^{13}C NMR spectra of PDIs were recorded in $CDCl_3$ using a Bruker Fourier 300HD NMR spectrometer. Elemental analysis was performed using a ThermoFlash EA 112 series instrument and a μ–Quant Microplate reader was used to obtain UV-Vis absorption spectra after filtering the suspensions using a 0.22 μm syringe filter. Particle size was measured using a Malvern Zetasizer.

2.3. Cell cytotoxicity and uptake of PDI nanoparticles. The evaluations of cell cytotoxicity were carried out by the ATP (adenosine triphosphate) assay on mesenchymal stromal cell line (mMSC D1, CRL-12424) which was obtained from ATCC and transduced with lentiviral particles

encoding firefly luciferase (Fluc) and ZsGreen or just ZsGreen under control of the constitutive promoter EF1a. MSCs were cultured in the medium comprised of Dulbecco's Modified Eagle Medium (DMEM, D6546, Sigma Aldrich), 10% fetal bovine serum (FBS, Gibco), 2mM L-glutamine (Sigma), 1% non-essential amino acids (Thermo Fisher), 0.1 mM 2-mercaptoethanol and 1% pen-strep at 37 °C under a humidified atmosphere with 5% CO_2. The CellTiter-Glo® assay (the commercial kit for ATP assay) was used to assess cell viability; MSCs were placed in a standard 96-well plate (2 x 10^5 cells/well) and left to attach and grow for 24 hours. After this, the culturing medium was replaced with fresh medium (200 µl) containing various concentrations of PDI nanoparticles (0-36 µg/ml). The assay was performed after incubating the MSCs for another 24 hours. To assess the effect of the PDI nanoparticles on MSC proliferation, cells were removed from the wells and counted using an automated cell counter (TC10, Biorad) at the culturing time of 24 h, 48 h, and 72 h. Confocal images were taken of fixed cell samples by Zeiss LSM 800 Airyscan. The flow cytometry analysis was carried out on live cell suspensions using a BD FACSCalibur. (See Supporting Information for more details on cell fixing, MSCs expressing ZsGreen, Mitomycin-C treatment, and flow cytometry).

2.4. In vivo Imaging. MSOT imaging of PDI-labelled MSCs in Agar phantoms was performed first (see Supporting Information for details on preparation of phantoms). For i*n vivo* imaging, MSCs were labelled with 15 µg/ml PDI nanoparticles for 24 hours. 1 x 10^6 MSCs were then suspended in 150 µl phosphate-buffered saline (PBS). The cell suspensions (1 x 10^6, 0.5 x 10^6, 0.25 x 10^6 PDI-labelled MSCs and 1 x 10^6 non-labelled MSCs) were then injected subcutaneously into four locations in the flanks of the mouse under anaesthetic condition. The immune-compromised nude CD1 mouse strain (female mice of 6-8 week old, bought from Charles River, UK) were used. The mice were imaged three times (day 1, day 7, day 11). Whole body

scans were performed with 1 mm steps in a rostro-caudal direction. 26 wavelengths (660 nm – 900 nm) were used for acquisition of images. On day 11 after the final imaging session, the mice were culled according to the Home Office guidelines.

All animal experiments were carried out under a license granted under the Animals (Scientific Procedures) Act 1986 and were approved by the University of Liverpool ethics committee. MSOT imaging was carried out using an inVision 256-TF small animal imaging system (iThera Medical GmbH) under anaesthetic condition for about 30 minutes, followed by imaging using the IVIS Spectrum (for bioluminescence and fluorescence measurements) for about 5 minutes under the same anaesthetic session. All photoacoustic data were reconstructed and multispectrally processed to unmix for the PDI spectra using ViewMSOT software.

2.5. Histology. Following animal sacrifice (on day 11), the MSC masses (visible to the naked eye) were surgically removed from the animals, fixed with 4% paraformaldehyde (24 h, 4°C), washed with PBS and soaked overnight in 30% sucrose (4°C). The tissues were cryo-embedded in OCT (Thermo Fisher) with dry ice and isopropanol, and stored at -80°C. Frozen cryostat sections were prepared by cutting at 7 µm thickness and stored at -20°C. Alizarin Red was then used to stain the MSC masses in order to detect the presence of calcium and check the potential of bone cell differentiation (see Supporting Information).

3. RESULTS AND DISCUSSION

3.1 Synthesis of PDI with NIR absorbance. PTCDA was used as the starting compound for the synthesis of NIR-active PDI. PTCDA is a highly hydrophobic dye and shows low solubility in most common solvents. In order to prepare the PDI with NIR absorbance and

suitable solubility, it is necessary to modify the PTCDA at the bay positions and the imide positions.[29, 30] Halogenated PDIs are effective starting building blocks for various PDIs. However, halogenation at the bay positions (usually with Br_2 or Cl_2) is generally performed in concentrated sulfuric acid at elevated temperatures.[25,29] Despite the harsh reaction conditions, a mixture of 1, 7-dihalogenated and 1, 6-dihalogenated perylene-based compounds is produced. We followed a method developed by Jager and co-authors to prepare regioisomerically pure brominated PTCDA under mild conditions,[45] which was then used to produce the PDI with NIR absorbance and better solubility in organic solvents including dichloromethane and acetone,[46] as shown in Figure 1 and Scheme S1.

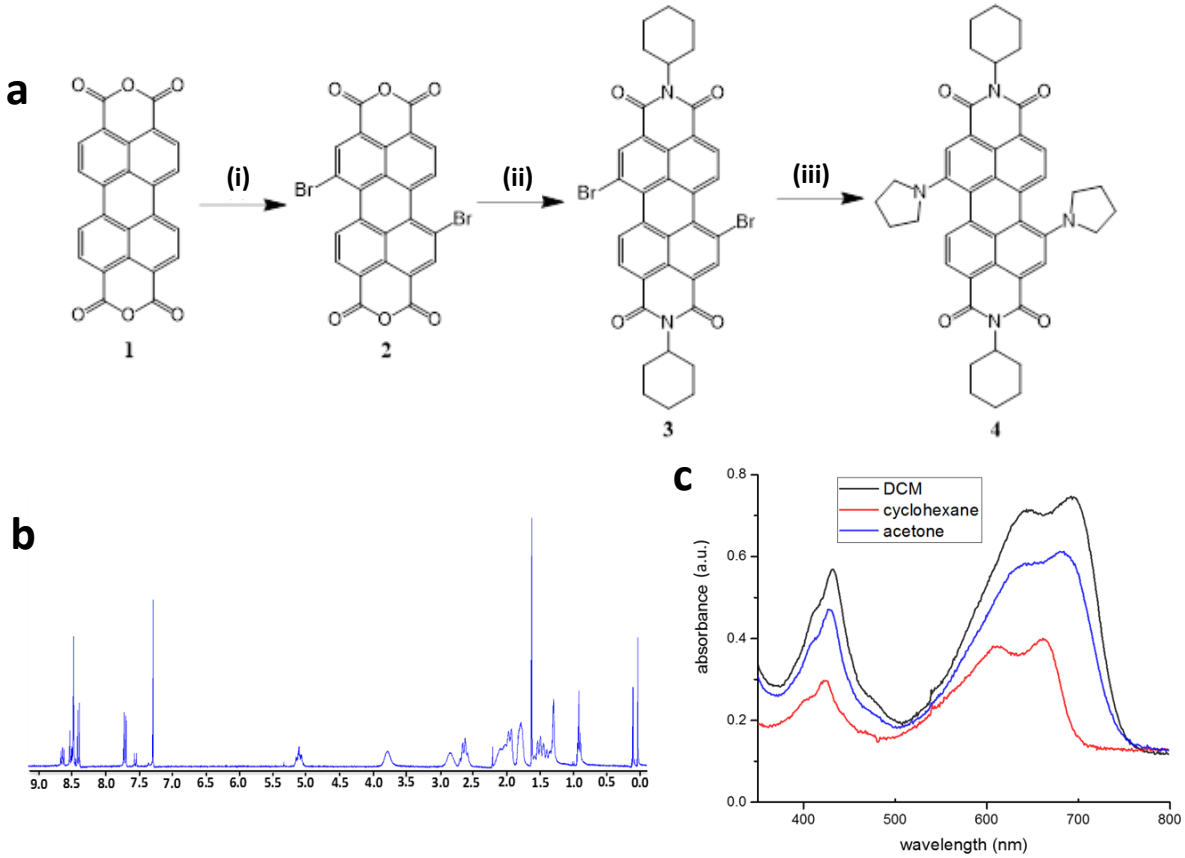

Figure 1. (a) The synthesis scheme for the preparation of the PDI with NIR absorbance (Compound 4). (i) Multiple steps detailed in Scheme S1. (ii) Reaction with cyclohexylamine in N-

methyl-2-pyrrolidinone with acetic acid, 85 ºC, N_2, 6 h. (iii) Pyrrolidine, N_2, 48 h, 65 °C. (b) ^{1}H NMR spectrum of the PDI (always referred to compound 4 if not specified). (c) UV-Vis profiles of the PDI solutions in different organic solvents with the same concentration (0.05 mg/ml).

Following the scheme illustrated in Figure 1a, the synthesis of compound 2 and the intermediate compounds is confirmed primarily by ^{1}H NMR spectroscopy with additional information from ^{13}C NMR and mass spectroscopy (Figures S1 – S3). The imide positions of compound 2 were then modified with cyclohexylamine to improve solubility in common solvents, followed by bay substitution of the bromine groups with pyrrolidine to achieve an NIR-absorbing PDI derivative **4**.[46]

The ^{1}H NMR spectrum confirms the formation of the PDI (compound 4, Figure 1b). Compared to compound 3 (Figure S4), the broad peaks at 3.8 ppm and 2.8 ppm are caused by the two differing hydrogen environments on the pyrrolidine rings. Some small peaks on the spectrum can be attributed to the impurities, which are still present after the recrystallization procedure. This is also reflected by the discrepancy of the elemental analysis data between the measured and calculated values of the PDI (Measured: C, 72.55%; H, 6.16%, N, 6.86%; Caculated: C, 76.25%; H, 6.42%; N, 8.09%). There is an obvious colour change from compound 3 to compound 4 – from orange red to dark green. This is also evidenced by the change of absorbance wavelength, i.e., the red shift from 528 nm to ~ 700 nm in dichloromethane (Figure S5).

The PDI (compound 4, which is referred as ‘PDI’ from now on) was found to show much better solubility in organic solvents including dichloromethane, acetone and cyclohexane (Figure 1c). The shapes of the UV-vis profiles are similar, but the peak positions are shifted for different solvents. Different absorbance intensity with the same concentration indicates different

absorbance coefficients. The strongest absorbance peaks of these solutions fall in the NIR region, with the wavelength being 662 nm for cyclohexane, 685 nm for acetone, and 695 nm for dichloromethane (DCM). This shows the PDI compound synthesized has the potential for PAI.

3.2. PDI nanoparticles. PDI is a hydrophobic compound and has very low solubility in water, hence cannot be used directly for bioimaging. However, it is possible to prepare an aqueous PDI nanoparticle suspension which can then be used for bioimaging. Aqueous organic nanoparticle suspensions can be readily prepared by nanoprecipitation.[32] In addition to the frequently used poly(vinyl alcohol) (PVA) as stabilizer, a SHBP with the structure of (DEAEMA$_{50}$-*c*-DEGDMA$_2$)-*b*-(OEGMA$_{80}$) was synthesized (Figure S6) and used as a stabilizer for PDI nanoparticles.

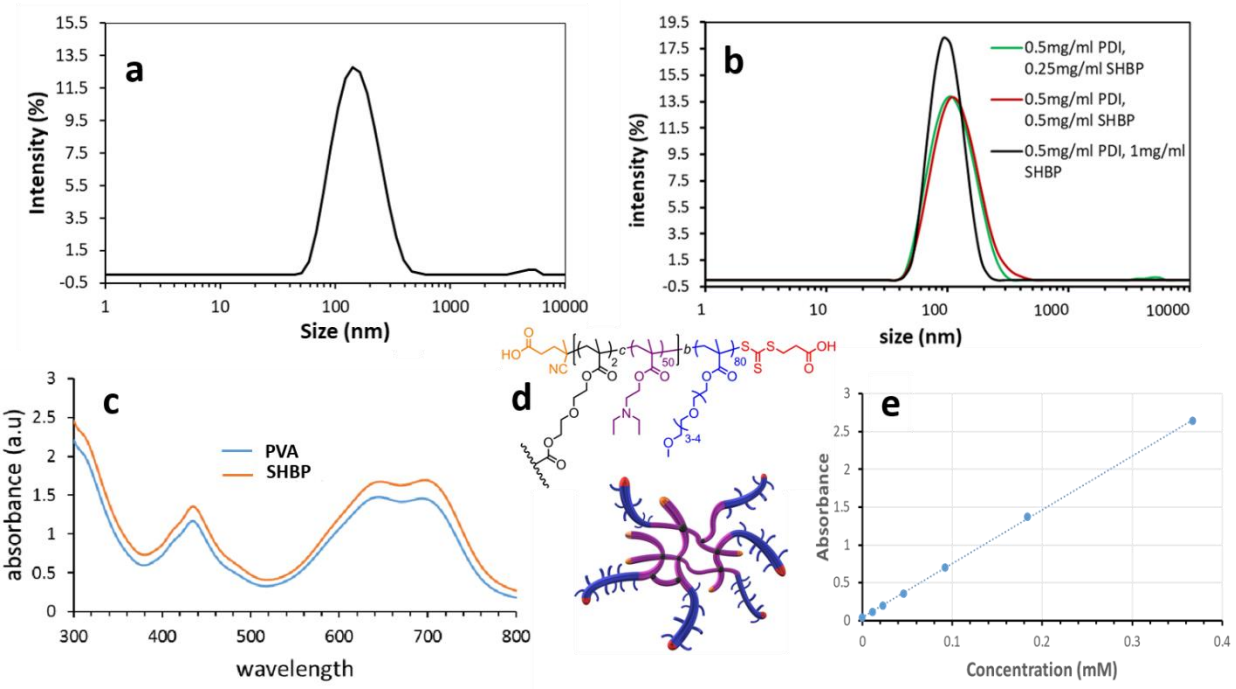

Figure 2. Characterization of PDI nanoparticles prepared by nanoprecipitation with PVA and SHBP as stabilizer. (a) DLS profile of PDI nanoparticles prepared with PVA as stabilizer at the mass ratio of PDI:PVA = 1:1. (b) DLS profiles of PDI nanoparticles prepared with SHBP as

stabilizer at the mass ratio of PDI:SHBP = 2:1, 1:1, and 1:2. (c) UV-vis profiles of PDI nanoparticles prepared with PVA and SHBP as stabilizers at the mass ratio of PDI:stabilizer = 1:1. (d) The molecular structure and schematic representation of the SHBP. (e) The graph shows the relationship of the absorbance of PDI nanoparticles (PDI:SHBP = 1:1 w/w) at wavelength of 705 nm versus PDI concentration, giving rise to a correlation equation $y = 7.107x + 0.041$, $R^2 = 0.9998$.

PDI nanoparticles were formed with both PVA and SHBP as stabilizers (at the mass ratio of PDI:stabilizer = 1:1), with particle diameters around 100 nm (in the range of 50 – 200 nm) as confirmed by dynamic laser scattering (DLS) analysis (Figure 2a, 2b). As seen in Figure 2c, the UV-Vis profiles of aqueous PDI nanoparticles with PVA and SHBP are similar. There is strong and broad absorbance in the range of 640 – 700 nm， similar to the profile obtained from the PDI-dichloromethane solution. More focused studies were carried out on the preparation of PDI nanoparticles using SHBP as stabilizer (Figure 2d) because it was found that PVA-stabilized PDI nanoparticles were not efficiently taken up by MSCs (discussed in section 3.3). Increasing the ratio of SHBP to PDI led to a narrower particle size distribution although the peak particle size was still around 100 nm (Figure 2b). The absorbance of PDI nanoparticles versus concentration was further investigated. As shown in Figure 2e, there was a linear concentration range of 0– 25 mg/ml (0 – 0.37 mM), giving a molar extinction coefficient of 17,901 M^{-1} cm^{-1}. For PDI nanoparticles with the mass ration of PDI:SHBP = 2:1, a higher molar extinction coefficient of 19,110 M^{-1} cm^{-1} was achieved, which could be attributed to the higher content of PDI in the nanoparticle suspension. However, the shape of the UV-vis profiles for the PDI nanoparticles with both ratios of PDI:SHBP was very similar (Fig. S7).

3.3. Biocompatibility and uptake of PDI nanoparticles in mouse MSCs. Mouse MSCs were labelled with varying concentrations of PDI nanoparticles with different stabilizers (SHBP and PVA, the mass ratio of PDI:stabilizer = 1:1) and tested in vitro to evaluate how PDI nanoparticles would impact cell viability and uptake efficiency. The mass ratio of PDI:stabilizer at 1:1 was selected for further investigation based on the balance of high nanoparticle stability and high PDI loading (hence higher extinction coefficient and signal intensity).

The uptake of PDI nanoparticles by MSCs was first assessed by incubating with PDI nanoparticles for 24 hours and then carrying out UV-vis analysis of the labelled cell suspensions. There were no absorbance peaks observed for PDI nanoparticles prepared with PVA as stabilizer despite the blue appearance of the cell pellet after centrifugation (Figure 3a). This suggests that the PVA-stabilized nanoparticles were not taken up by the MSCs.

The MSCs labelled with SHBP-stabilized PDI nanoparticles had absorbance around 700 nm, with the intensity increasing as the dosing concentration was increased to 13.6 μg/ml (Figure 3b). The peak intensity at 700 nm decreased when the PDI concentration was further increased to 27.2 μg/ml. The high uptake of SHBP-stabilized PDI nanoparticles by MSCs can be attributed to the unique molecular structure of the SHBP (Figure 2d). The SHBP is comprised of many covalently cross-linked linear diblock copolymer chains containing both a hydrophobic section and a hydrophilic section which provides several advantages: multivalent stabilization, dendritic solubilization, and high molecular weight. While the hydrophobic section is anchored to the PDI nanoparticles to offer stabilization, the hydrophilic chains are likely to extend out from the nanoparticle surface to facilitate cell interactions and cell uptake.[47] In comparison, a simple hydrophilic linear polymer chain, like the PVA used in this study, is weakly attached to the

hydrophobic nanoparticles. There is no polymer chains protruding from the particle surface to interact with the cells. Any excess PVA would be dissolved in the aqueous medium.

The stability of PDI nanoparticles in cell culture medium (containing different ions and biomacromolecules) is highly important for biomedical studies.[48] However, the characterization of PDI nanoparticles in culture medium in our study did not produce reliable results by DLS and electronic microscopy, which was likely due to the presence of biomacromolecules and the low atomic contrast between PDI nanoparticles and biomacromolecules (both organic). However, there was no observation of PDI nanoparticles aggregation during the culturing period, which could be attributed to the excellent stabilization by SHBP.

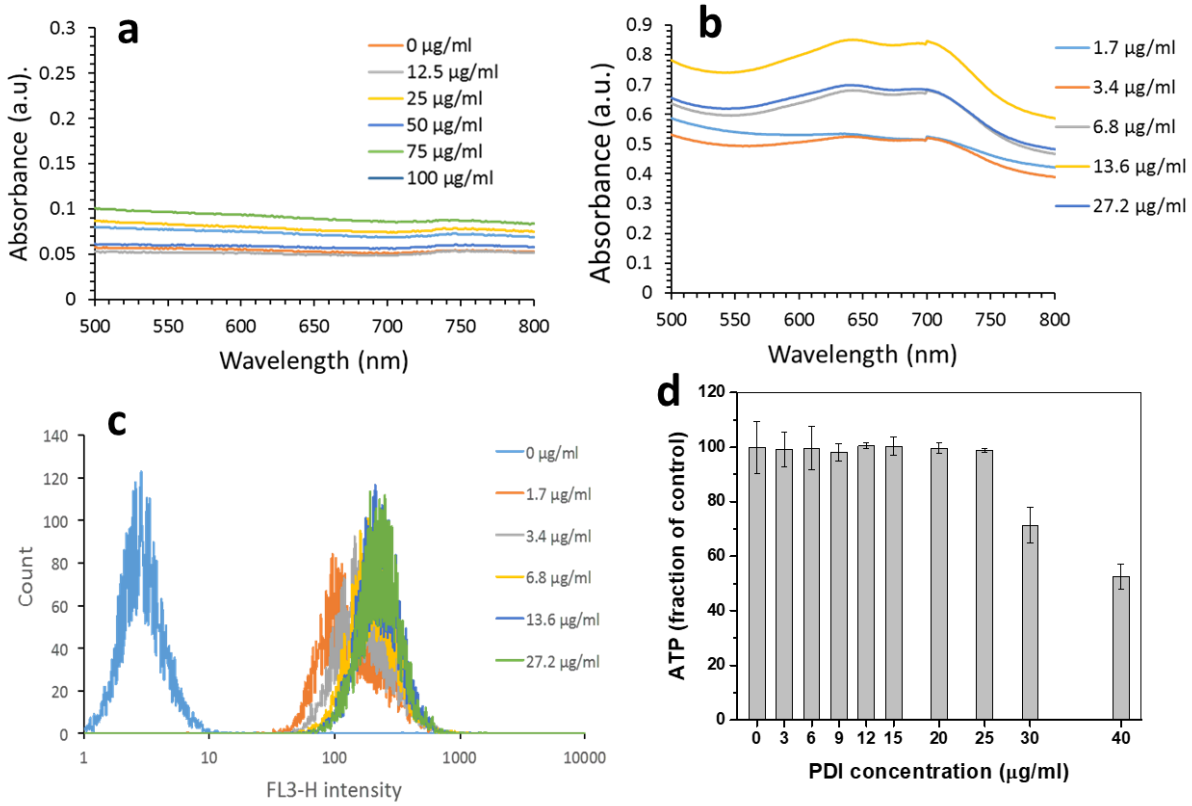

Figure 3. *In vitro* evaluation of PDI nanoparticles by culturing with MSCs for 24 hours. UV-vis profiles of the MSC suspensions in PBS after culturing with PVA-stabilized PDI nanoparticles (a) and SHBP-stabilized PDI nanoparticles (b). (c) The flow cytometry analysis shows the intensity change of SHBP-PDI-labelled MSCs under the same culturing conditions as in (b). (d) Evaluation of cell cytoxicity based on ATP generation with SHBP-stabilized PDI nanoparticles. The bars indicate the mean value per group around the standard deviation (error bars, in the range of 0.6 – 9.5 %, each experiment repeated 3 times).

The fluorescence property of the PDI (fluorescence maxima wavelength 734 nm and quantum yield of 0.21 in CH_2Cl_2)[46] suggested that it was possible to characterize the presence of PDI nanoparticles by fluorescence-related techniques, e.g., flow cytometry. As such, the uptake of SHBP-stabilized PDI nanoparticles was further confirmed by analysis using flow cytometry, where an increase in intensity at 670 nm was observed with increasing dose concentration of PDI nanoparticles up to 13.6 μg/ml (Figure 3c). Further increase in PDI concentration (up to 27.2 μg/ml) did not lead to further increases in intensity, indicating that the PDI concentration could be saturated beyond this point. This suggests that the uptake of PDI nanoparticles is optimal at 13.6 μg/ml under our testing conditions, i.e., the highest uptake per unit cell. This concentration resulted in greater MSOT signal intensity because of the high uptake in the MSCs. Therefore, for all MSOT imaging experiments, MSC labelling was performed in the culture medium containing PDI nanoparticles (15 μg/ml, with the ratio of PDI:SHBP = 1:1 w/w).

The cytotoxicity of PDI nanoparticles when cultured with MSCs was assessed by the ATP assay against the MTT (3-[4,5-dimethylthiazol-2-diphenyl] tetrazolium bromide) assay. There were some issues with the MTT assay when testing the cytotoxicity of other nanoparticles

in previous studies,[49] with the reason being mainly interference of the nanoparticles with the MTT assay components whilst ATP assay is accepted as the more sensitive, fast, and reliable method for evaluating cytotoxicity.[50,51] MSCs were dosed with increasing concentrations of PDI nanoparticles (range 0 – 50 μg/ml) and their effect on cell health was assessed by measuring levels of ATP production.[49] The initial assessments showed neither types of PDI nanoparticles had effect on ATP production with PDI nanoparticle concentrations up to 25 μg/ml. However, because of the low uptake of PVA-stabilized PDI nanoparticles by the MSCs, further studies were focused on SHBP-stabilized PDI nanoparticles. Figure 3d shows the ATP production of PDI-labelled MSCs was around 100% up to the PDI concentration of 25 μg/ml. The ATP production decreased considerably when the PDI concentration was increased further. Proliferation of the MSCs labelled with the PDI nanoparticles at the concentration of 25 μg/mL was compared with non-labelled MSCs. It was found that the proliferation of the MSCs was not negatively impacted by the uptake of PDI nanoparticles (Fig. S8), demonstrating the high biocompatibility of SHBP-stabilized PDI nanoparticles.

3.4. Fate of PDI nanoparticles after uptake by MSCs. What happened to the PDI nanoparticle after being taken up by the MSCs is an important question. Did the PDI nanoparticles remain inside the MSCs or were they exocytosed into the medium? In the latter case, the result would show decreasing signal intensity in the cells due to there being fewer PDI nanoparticles. This would suggest that the particles are not useful for cell tracking *in vivo*, because in addition to the reduced signal intensity, there could be problems with false positive results if the particles were taken up by host cells.

To investigate if there was any evidence of exocytosis, the MSCs labelled with PDI nanoparticles were co-cultured with non-labelled MSCs that expressed the green fluorescence protein, ZsGreen. If any of the ZsGreen-expressing cells were to become labelled with the PDI nanoparticles, this would suggest that the particles could be exocytosed and then taken-up by neighboring cells. It was observed that none of the ZsGreen-expressing cells in the co-culture became labelled with PDI nanoparticles (Figure S9), indicating that the particles would be unlikely to generate false positive results in cell tracking experiments.

To confirm that the PDI nanoparticles were not exocytosed from the MSCs, following labelling, MSCs were either left untreated (control group), or exposed to Mitomycin-C, which is a drug that prevents cells from proliferating. We would anticipate that over a few days, the fluorescence intensity of control MSCs would decrease, due to the nanoparticle load being reduced by 50% per cell with each cell division. On the other hand, in the Mitomycin-C treated non-proliferating cells, any loss in fluorescence could suggest that exocytosis was taking place. As shown in Figure 4a, for PDI-labelled MSCs without Mitomycin-C treatment, the fluorescence intensity of the cells has decreased significantly from the labelled cells (intensity 300) to culturing for 2 days (intensity 105) and for 4 days (intensity 10) whilst the fluorescence intensity for non-labelled cells is just 3. (Please note: The unit is arbitrary for the values of fluorescence intensity and these values are just for comparison purpose.). However, no loss of fluorescence intensity was observed in the Mitomycin-C treated group, even at 2 weeks following labelling (Figure 4b). Considering all these results, it suggests that the PDI nanoparticles are not exocytosed from the MSCs, thus confirming that the PDI nanoparticles are contained inside the MSCs after uptake. The reason is believed to be the stabilizing effect of SHBP on PDI

nanoparticles and strong interaction of SHBP with the surrounding environment after SHBP-stabilized PDI nanoparticles are taken up by the MSCs.[47]

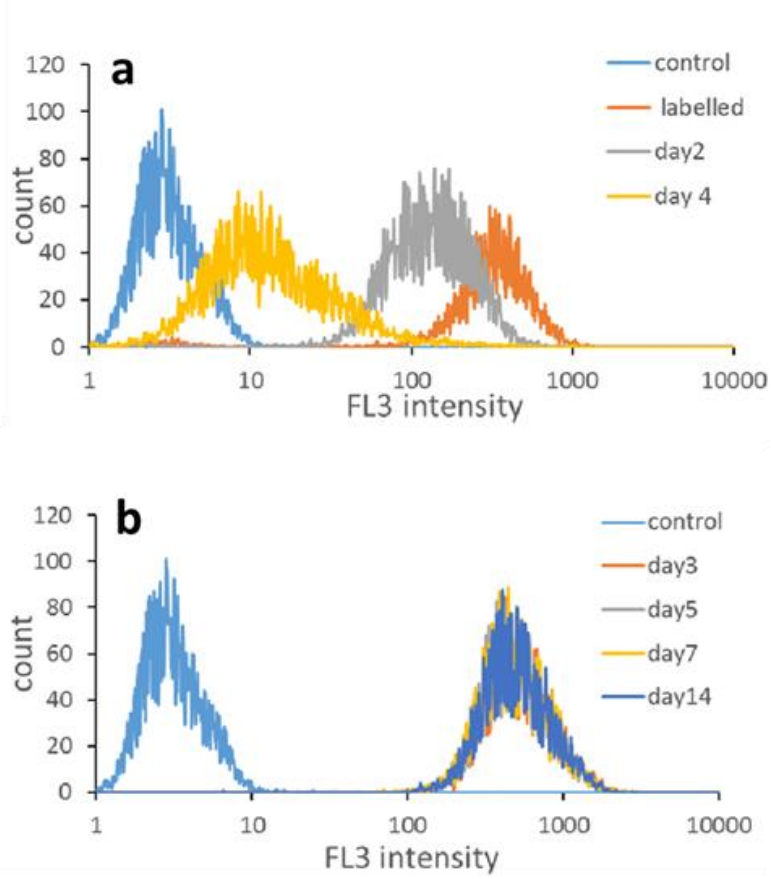

Figure 4. Flow cytometry analysis of MSCs labelled with SHBP-stabilized PDI nanoparticles, which are further treated under different conditions. (a) The MSCs cultured in PDI-containing medium for 1 day (the 'labelled' sample), then further cultured in a fresh PDI-free medium for a further 24 h (sample 'day 2') or 72 h (sample 'day 4'). (b) Labelled MSCs treated with Mitomycin-C and then cultured in PDI-free medium for 14 days. Non-labelled MSCs are used as the control.

3.5. Evaluation of PDI nanoparticles as PAI (MSOT) probes. The broad and strong NIR absorbance of PDI nanoparticles implies that they are suitable for PAI, particularly MSOT imaging. PDI-labelled MSCs were first imaged in a phantom with MSOT in order to show their

potential for *in vivo* imaging. MSC suspensions (PDI-labelled and non-labelled, 1 x 10^5 cells in 150 µl PBS) were injected into channels within an agar phantom. The MSOT image clearly revealed the PDI-labelled MSCs (red) while the non-labelled cells could not be detected (Figure S10).

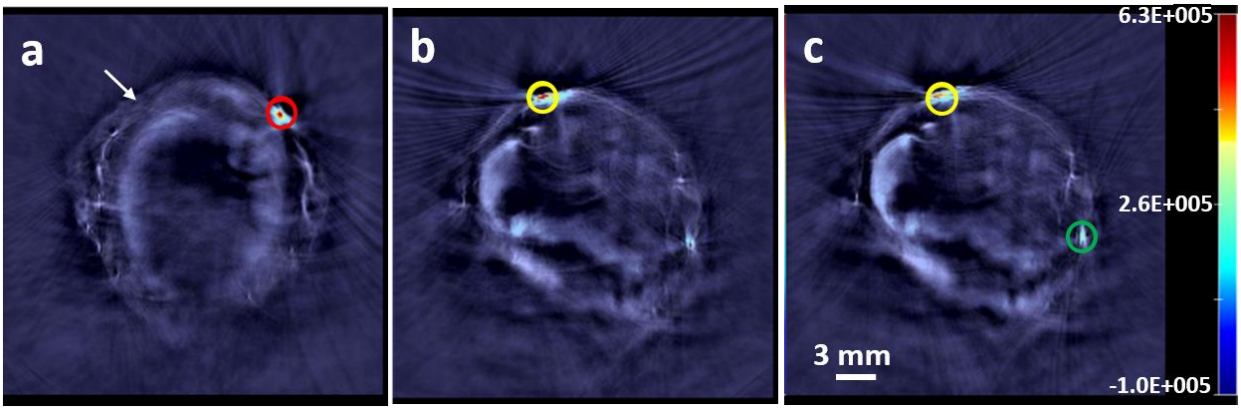

Figure 5. Axial MSOT images of a mouse taken 1 day post-administration with PDI-labelled MSCs, where the red (a), yellow (b,c) and green circles (c) respectively indicate the spots 1 x 10^6, 0.5 x 10^6 and 0.25 x 10^6 PDI-labelled MSCs. The white arrow indicates the position of non-labelled MSCs. The same length scale bar and colour scale bar are used for all the images.

For *in vivo* imaging, PDI-labelled MSCs expressing Fluc and ZsGreen were injected subcutaneously into four locations in the flanks of the mouse. PDI-labelled MSCs were injected at the amounts of 1 x 10^6, 0.5 x 10^6 or 0.25 x 10^6 cells while non-labelled MSCs (1 x 10^6) were injected and served as a control. The torso of the mouse was imaged on day 1 in 1 mm intervals in a rostro-caudal direction. The PDI-labelled MSCs could be detected while no signal was detected from non-labelled MSCs (Fig. S11). Figure 5 shows representative MSOT images of the PDI-labelled MSCs. It is clear that the most intense signal was generated by the highest number of PDI-labelled MSCs (1 x 10^6 cells). However, the lowest number of PDI-labelled MSCs (0.25

x 10^6 cells) could still be detected by MSOT. The same scans were performed 7 and 11 days after injecting the labelled MSCs. MSOT images of similar quality on day 11 were obtained (Fig. S12, Fig. S13).

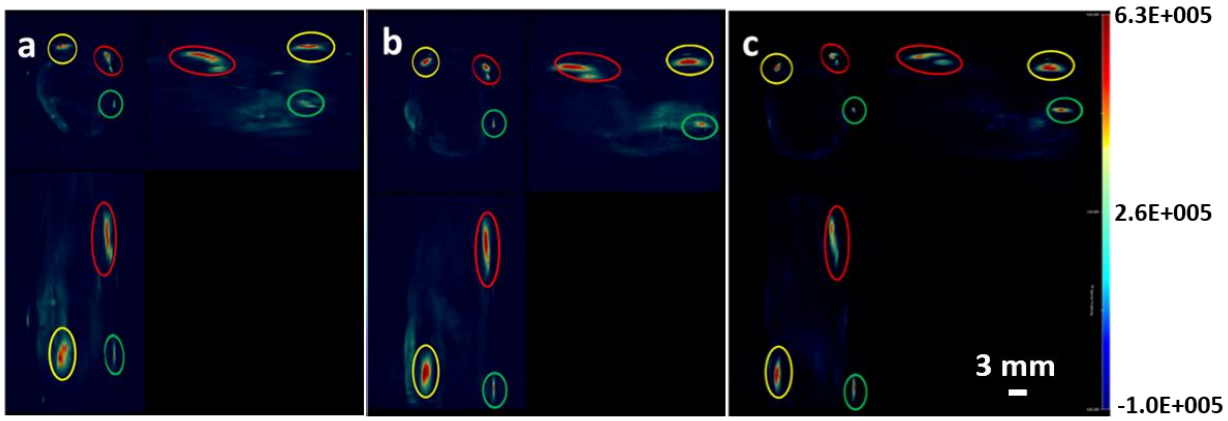

Figure 6. MSOT 3D view of mouse after injection with MSCs on: a) day 1, b) day 7 and c) day 11. Each panel shows the three cross-section view: top left, transverse plane; top right, sagittal plane; bottom left, coronal plane. Red circles indicate 1 x 10^6 PDI-labelled cells, yellow circles indicate 0.5 x 10^6 PDI-labelled cells, and green circles indicate 0.25 x 10^6 PDI-labelled cells. The cell locations are determined based on PDI signal intensity after spectrally unmixing. All these images utilise the same length scale bar and colour scale bar.

3D images were created with the ViewMSOT software and three cross-sections are shown for each imaging times, *i.e.,* day 1, day 7 and day 11, in Figure 6. The three injected PDI-labelled MSC masses in the 3D views were observed at the expected locations in the mouse, with the highest number of injected cells giving the most intense signal throughout the imaging period from day 1 to day 11. These results show the potential of the PDI nanoparticles as MSOT probes for long-term cell tracking.

Bioluminescence imaging was further used to confirm whether the cells were viable and proliferating. The strong and increasing signals over time by the luminescent radiance in Figure 7a-c demonstrate that the PDI-labelled MSCs remained viable and were able to proliferate. It should be noted that in contrast to the MSOT images, the bioluminescence image is only planar and has poor spatial resolution. However, the use of bioluminescence was also essential for avoiding false positives in vivo. If the PDI-labelled MSCs were to undergo apoptosis, host macrophages would engulf the cell debris along with any released NPs, and hence a possibility of false positives by MSOT. If that happened, the bioluminescence signals from the MSCs would be lost or reduced. Since the bioluminescence signal intensity increased with time (Fig. 7a-c), this indicates it is unlikely to generate false positives upon cell death.

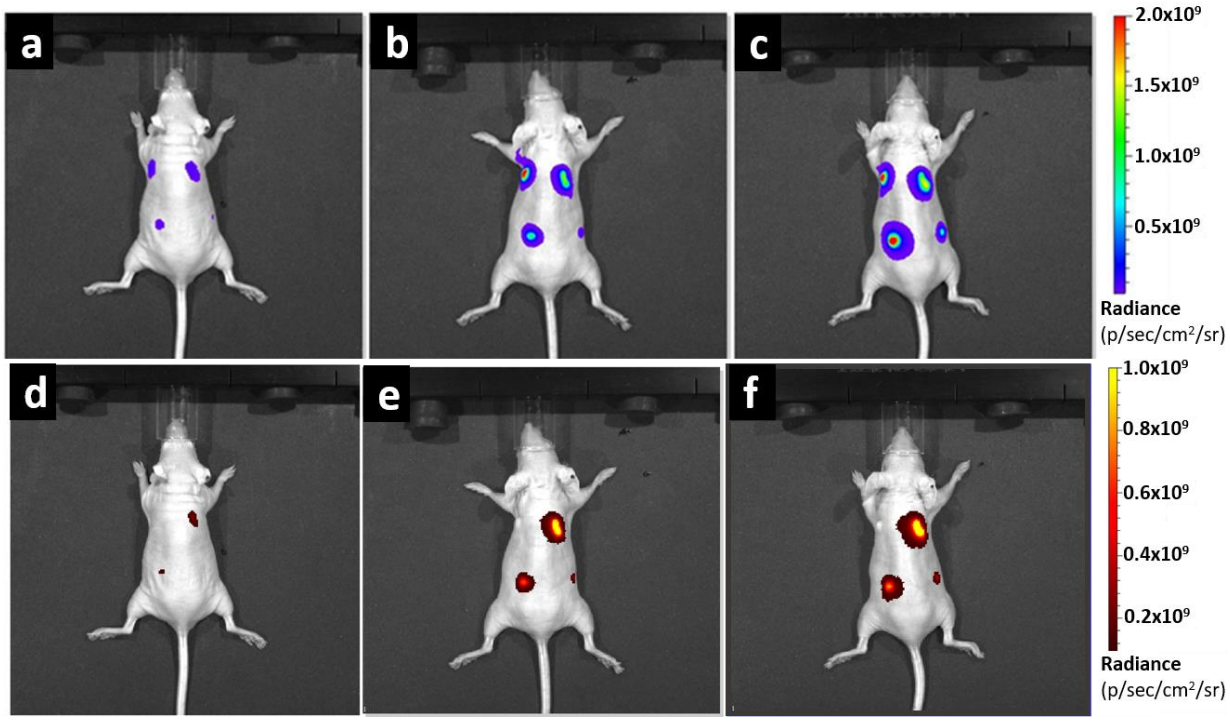

Figure 7. Bioluminescence (a-c) and fluorescence imaging (d-f) of the mouse subcutaneously injected with MSCs: (a,d) day 1; (b,e) day 7; (c,f) day 11. Imaging spots: top left, non-labelled

MSCs; top right: PDI-labelled MSCs, 1 x 10^6 cells; bottom left, PDI-labelled MSCs, 0.5 x 10^6 cells; bottom right, PDI-labelled MSCs, 0.25 x 10^6 cells.

Since PDI nanoparticles also exhibit fluorescence properties, fluorescence imaging was employed to determine if the PDI-labelled MSCs generated sufficient signal to be detected by fluorescence imaging. On imaging of day 1, fluorescent spots were clearly visible for the two areas that were implanted with the larger numbers of PDI-labelled MSCs, with the area injected with 1 x10^6 PDI-labelled MSCs generating a more intense signal than the area injected with 0.5 x 10^6 PDI-labelled MSCs (Figure 7d). For the area injected with the lowest number of cells (2.5 x 10^5 cells), the signal could not be identified from background, indicating that *in vivo* fluorescence imaging of the PDI-labelled cells is not as sensitive as MSOT. As expected, no fluorescence signal was detected for the non-labelled MSCs (Figure 7d). Surprisingly, the fluorescence intensity increased with time (day 7 and day 11 imaging, Figures 7e-f) while there was still no signal from the non-labelled MSCs. It is speculated that the bioluminescence released from the cells may enhance fluorescent intensity of the PDI nanoparticles via a bioluminescence resonance energy transfer (BRET) process (where small distance ($\leq$ 10 nm) is required between bioluminescent donor and fluorescent acceptor)[52] or a conventional radiating (where fluorescence is caused by unbound excitation from luminescence).[53] In this event, the increasing bioluminescence from day 1 – day 11 would lead to intensified fluorescence signal. A control experiment, by fluorescence imaging of the implanted MSCs without firefly luciferase labelling, is proposed for future study and will be likely to confirm this explanation. Overall, these observations indicate that MSOT is superior to fluorescence imaging for indicating the precise position of PDI-labelled cells, and is also a more sensitive technique, as it enables fewer

numbers of cells to be detected than with fluorescence imaging. Ideally, for *in vivo* cell tracking, it is optimal to combine bioluminescence (firefly luciferase) with MSOT (PDI nanoparticles), because this allows the viability and proliferation of the cells to be monitored with bioluminescence, while at the same time allowing them to be precisely located with MSOT.

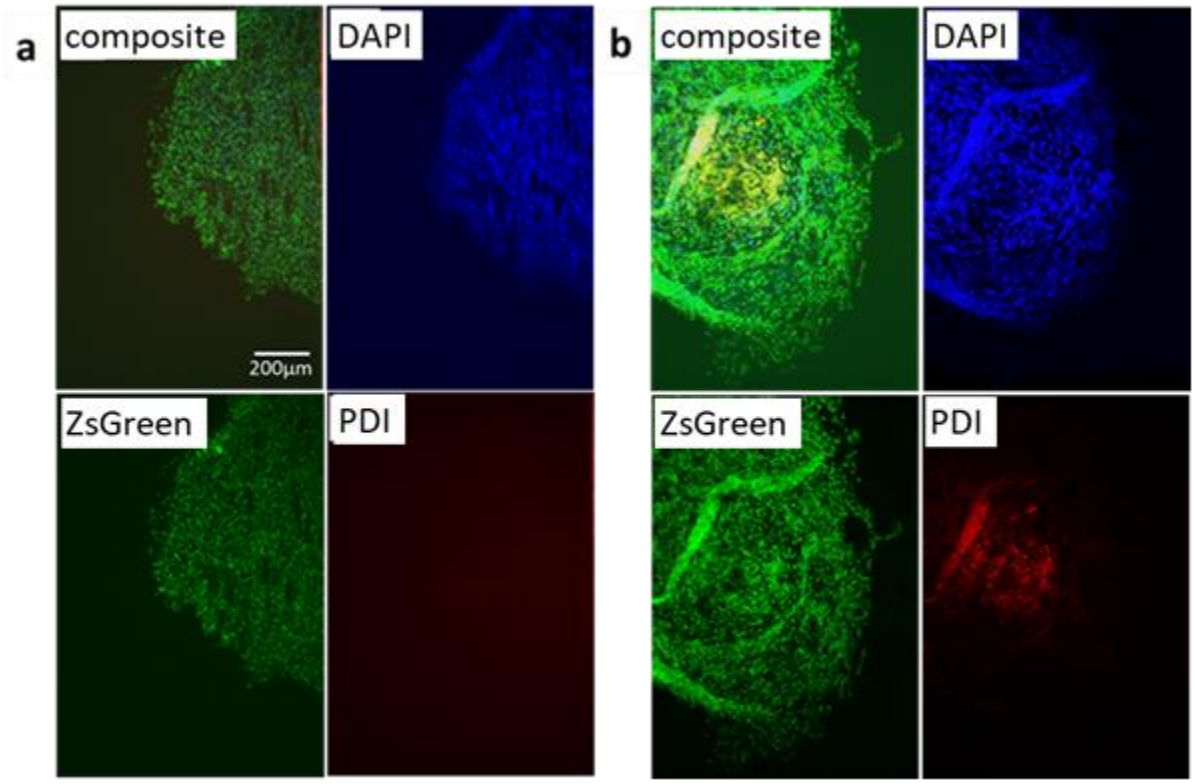

Figure 8. Confocal microscope images of frozen sections of dissected MSC masses co-stained with DAPI (blue), where green colour is from ZsGreen expressing MSCs and red fluorescence is from PDI nanoparticles. (a) Non-labelled MSC masse does not show any red fluorescence; (b) PDI-labelled MSCs masse shows red fluorescence from PDI nanoparticles. The difference between non-labelled and labelled MSC masses is also visible in the composite image.

Immunofluorescence was also carried out on frozen sections of dissected MSC masses, where the MSCs could be detected due to their expression of ZsGreen. Frozen sections (7 µm in

thickness) of the MSC masses were fixed with paraformaldehyde, stained with DAPI and imaged by confocal microscopy (Figure 8). The MSC mass derived from non-labelled MSCs did not display any red fluorescence whilst the MSC masses derived from PDI-labelled MSCs displayed a central area of red fluorescence. The yellowish feature in the composite image was also visible for PDI-labelled MSCs, as a result of composition with red fluorescence. This provides further evidence that staining of MSCs with PDI nanoparticles does not adversely affect cell proliferation and the imaging potential of PDI can be used for both MSOT and fluorescence imaging.

MSCs were reported to show a propensity to differentiate into osteocytes and cartilage when injected subcutaneously into mice.[54] Thus, in the present study, histological analysis was used to confirm the presence of calcium in both non-labelled and PDI-labelled samples, indicating that the PDI probes do not affect the differentiation capabilities of the MSCs (Fig. S14).

4. CONCLUSIONS

PDI nanoparticles as near-infrared absorbing probes are prepared and evaluated for *in vivo* tracking of MSCs using MSOT. The PDI nanoparticles are formed by nanoprecipitation using a star hyperbranched polymer ($DEAEMA_{50}$-*c*-$DEGDMA_2$)-*b*-($OEGMA_{80}$), with a particle size of around 100 nm and good stability in aqueous medium. The PDI nanoparticles show excellent uptake into MSCs with no noticeable effect on cell viability up to concentrations of 25 μg/ml. The PDI-labelled MSCs are injected into the flanks of mice where the probes can be clearly visualized up to 11 days post-administration with MSOT. The high sensitivity of MSOT allows for the detection of fewer numbers of cells than with fluorescence imaging. PDI nanoparticles can be used in

conjunction with bioluminescence imaging to assess cell viability and proliferation, in order to aid the development of regenerative medicine therapies.

ASSOCIATED CONTENT

Supporting Information. The Supporting Information is available free of charge at https://pubs.acs.org.

Detailed experimental procedures, synthesis scheme of brominated PTCDA, NMR spectra of PDIs, UV-vis profiles of PDI in dichloromethane & PDI nanoparticle suspensions, cell proliferation graph, bioimaging graphs, and histology of MSC masses (PDF).

AUTHOR INFORMATION

Corresponding Author

*Email: zhanghf@liverpool.ac.uk

ORCID

Haifei Zhang: 0000-0001-5142-5824

Author Contributions

The manuscript was written through contributions of all authors. All authors have given approval to the final version of the manuscript.

Notes

The authors declare no competing financial interest.

ACKNOWLEDGMENT

Y.Y. and C.F. acknowledged the PhD studentships from the EPSRC. U.W. was grateful for the joint PhD studentship between the University of Liverpool and Singapore A*STAR.

REFERENCES

(1) Satija, N. K.; Singh, V. K.; Verma, Y. K.; Gupta, P.; Sharma, S.; Afrin, F.; Sharma, M.; Sharma, P.; Tripathi, R. P.; Gurudutta, G. U. Mesenchymal Stem Cell-Based Therapy: A New Paradigm in Regenerative Medicine. *J. Cell. Mol. Med.* **2009**, *13*, 4358-4402.

(2) Bianco, P.; Cao, X.; Frenette, P. S.; Mao, J. J.; Robey, P. G.; Simmons, P. J.; Wang, C.-Y. The Meaning, the Sense and the Significance: Translating the Science of Mesenchymal Stem Cells into Medicine. *Nat. Med.* **2013**, *19*, 35-42.

(3) Freitag, J.; Bates, D.; Boyd, R. L.; Shah, K.; Barnard, A.; Huguenin, L.; Tenen, A. Mesenchymal Stem Cell Therapy in the Treatment of Osteoarthritis: Reparative Pathways, Safety and Efficacy - A Review. *BMC Musculoskelet. Disord.* **2016**, *17*, 230.

(4) Carvello, M.; Lightner, A.; Yamamoto, T.; Kotze, P. G.; Spinelli, A. Mesenchymal Stem Cells for Perianal Crohn's Disease. Cells **2019**, *8*, 764.

(5) Scarfe, L.; Brillant, N.; Kumar, J. D.; Ali, N.; Alrumayh, A.; Amali, M.; Barbellion, S.; Jones, V.; Niemeijer, M.; Potdevin, S.; Roussignol, G.; Vaganov, A.; Barbaric, I.; Barrow, M.; Burton, N. C.; Connell, J.; Dazzi, F.; Edsbagge, J.; French, N. S.; Holder, J.; Hutchinson, C.; Jones, D. R.; Kalber, T.; Lovatt, C.; Lythgoe, M. F.; Patel, S.; Patrick, P. S.; Piner, J.; Reinhardt, J.; Ricci, E.; Sidaway, J.; Stacey, G. N.; Lewis, P. J. S.; Sullivan, G.; Taylor, A.; Wilm, B.; Poptani, H.; Murray, P.; Goldring, C. E. P.; Park, B. K. Preclinical Imaging Methods for Assessing the Safety and Efficacy of Regenerative Medicine Therapies. *NPJ Reg. Med.* **2017**, *2*, 28.

(6) Knoepfler, P. S. Deconstructing Stem Cell Tumorigenicity: A Roadmap to Safe Regenerative Medicine. *Stem Cells* **2009**, *27*, 1050-1056.

(7) Sharkey, J.; Scarfe, L.; Santeramo, I.; Garcia-Finana, M.; Park, B. K.; Poptani, H.; Wilm, B.; Taylor, A.; Murray, P. Imaging Technologies for Monitoring the Safety, Efficacy and Mechanisms of Action of Cell-Based Regenerative Medicine Therapies in Models of Kidney Disease. *Eur. J. Pharmacol.* **2016**, *790*, 74-82.

(8) James, M. L.; Gambhir, S. S. A Molecular Imaging Primer: Modalities, Imaging Agents, and Applications. *Physiol. Rev.* **2012**, *92*, 897-965.

(9) Wang, L.V.; Hu, S. Photoacoustic tomography: in vivo imaging from organelles to organs. *Science* **2012**, 335, 1458-1462.

(10) Gujrati, V.; Mishra, A.; Ntziachristos, V. Molecular Imaging Probes for Multi-Spectral Optoacoustic Tomography. *Chem. Commun.* **2017**, *53*, 4653 – 4672.

(11) Comenge, J.; Sharkey, J.; Fraguiero, O.; Wilm, B.; Brust, M.; Murray, P.; Levy, R.; Plagge, A. Multimodal Cell Tracking from Systemic Administration to Tumour Growth by Combining Gold Nanorods and Reporter Genes. *eLife* **2018**, *7*, e33140.

(12) Razansky, D. ; Distel, M.; Vinegoni, C.; Ma, R.; Perrimon, N.; Köster, R. W.; Ntziachristos, V. Multispectral Opto-Acoustic Tomography of Deep-Seated Fluorescent Proteins in Vivo. *Nat. Photonics* **2009**, *3*, 412-417.

(13) Taruttis, A.; Morscher, S.; Burton, N. C.; Razansky, D.; Ntziachristos, V. Fast Multispectral Optoacoustic Tomography (MSOT) for Dynamic Imaging of Pharmacokinetics and Biodistribution in Multiple Organs. *PLOS One* **2012**, *7*, e30491.

(14) Weber, J.; Beard, P.; Bohndiek, S. E. Contrast Agents for Molecular Photoacoustic Imaging. *Nat. Methods* **2016**, *13*, 639 – 650.

(15) Ge, X.; Fu, Q.; Bai, L.; Chen, B.; Wang, R.; Gao, S.; Song, J. Photoacoustic Imaging and Photothermal Therapy in the Second Near-Infrared Window. *New J. Chem.* **2019**, *43*, 8835-8851.

(16) Upputuri, P. K.; Pramanik, M. Recent Advances in Photoacoustic Contrast Agents for in Vivo Imaging. *WIREs Nanomed. Nanobiotechnol.* **2020**, e1618.

(17) Comenge, J.; Fragueiro, O.; Sharkey, J.; Taylor, A.; Held, M.; Burton, N. C.; Park, B. K.; Wilm, B.; Murray, P.; Brust, M.; Lévy, R. Preventing Plasmon Coupling between Gold Nanorods Improves the Sensitivity of Photoacoustic Detection of Labeled Stem Cells in Vivo. *ACS Nano* **2016**, *10*, 7106-7116.

(18) Borg, R. E.; Rochford, J. Molecular Photoacoustic Contrast Agents: Design Principles & Applications. *Photochem. Photobiol.* **2018**, *94*, 1175-1209.

(19) Yang, X.; Stein, E. W.; Ashkenazi, S.; Wang, L. V. Nanoparticles for Photoacoustic Imaging. *WIREs Nanomed. Nanobiotechnol.* **2009**, *1*, 360-368.

(20) Maturi, M.; Locatelli, E.; Monaco, I.; Franchini, M. C. Current Concepts in Nanostructured Contrast Media Development for in Vivo Photoacoustic Imaging. *Biomater. Sci.* 2019, 7, 1746 – 1775.

(21) Pu, K.; Shuhendler, A. J.; Jokerst, J. V.; Mei, J.; Gambhir, S. S.; Bao, Z.; Rao, J. Semiconducting Polymer Nanoparticles as Photoacoustic Molecular Imaging Probes in Living Mice. *Nature Nanotechnol.* **2014**, *9*, 233-239.

(22) Jiang, Y.; Pu, K. Advanced Photoacoustic Imaging Applications of Near-Infrared Absorbing Organic Nanoparticles. *Small* **2017**, *13*, 1700710.

(23) Li, K.; Liu, B. Polymer-Encapsulated Organic Nanoparticles for Fluorescence and Photoacoustic Imaging. *Chem. Soc. Rev.* **2014**, *43*, 6570-6597.

(24) Guo, B.; Chen, J.; Chen, N.; Middha, E.; Xu, S.; Pan, Y.; Wu, M.; Li, K.; Liu, C.; Liu, B. High-Resolution 3D NIR-II Photoacoustic Imaging of Cerebral and Tumor Vasculatures Using Conjugated Polymer Nanoparticles as Contrast Agent. *Adv. Mater.* **2019**, 1808355.

(25) Huang, C.; Barlow, S.; Marder, S. R. Perylene-3,4,9,10-tetracarboxylic Acid Diimides: Synthesis, Physical Properties, and Use in Organic Electronics. *J. Org. Chem.* **2011**, *76*, 2386-2407.

(26) Li, C.; Wonneberger, H. Perylene Imides for Organic Photovoltaics: Yesterday, Today, and Tomorrow. *Adv. Mater.* **2012**, *24*, 613-636.

(27) Avlasevich, Y.; Li, C.; Müllen, K. Synthesis and Applications of Core-Enlarged Perylene Dyes. *J. Mater. Chem.* **2010**, *20*, 3814-3826.

(28) Chen, L.; Li, C.; Müllen, K. Beyond Perylene Diimides: Synthesis, Assembly and Function of Higher Rylene Chromophores. *J. Mater. Chem. C* **2014**, *2*, 1938-1956.

(29) Würthner, F.; Saha-Möller, C. R.; Fimmel, B.; Oqi, S.; Leowanawat, P.; Schmidt, D. Perylene Bisimide Dye Assemblies as Archetype Functional Supramolecular Materials. *Chem. Rev.* **2016**, *116*, 962-1052.

(30) Chen, S.; Slattum, P.; Wang, C.; Zang, L. Self-Assembly of Perylene Imide Molecules into 1D Nanostructures: Methods, Morphologies, and Applications. *Chem. Rev.* **2015**, *115*, 11967-11998.

(31) Ji, C.; Cheng, W.; Yuan, Q.; Müllen, K.; Yin, M. From Dyestuff Chemistry to Cancer Theranostics: The Rise of Rylenecarboximides. *Acc. Chem. Res.* **2019**, *52*, 2266-2277.

(32) Fan, Q.; Cheng, K.; Yang, Z.; Zhang, R.; Yang, M.; Hu, X.; Ma, X.; Bu, L.; Lu, X.; Xiong, X.; Huang, W.; Zhao, H.; Cheng, Z. Perylene-Diimide-Based Nanoparticles as Highly Efficient Photoacoustic Agents for Deep Brain Tumor Imaging in Living Mice. *Adv. Mater.* **2015**, *27*, 843-847.

(33) Yang, Z.; Tian, R.; Wu, J.; Fan, Q.; Yung, B. C.; Niu, G.; Jacobson, O.; Wang, Z.; Liu, G.; Yu, G.; Huang, W.; Song, J.; Chen, X. Impact of Semiconducting Perylene Diimide Nanoparticle Size on Lymph Node Mapping and Cancer Imaging. *ACS Nano* **2017**, *11*, 4247-4255.

(34) Sun, P.; Wang, X.; Wang, G.; Deng, W.; Shen, Q.; Jiang, R.; Wang, W.; Fan, Q.; Huang, W. A Perylene Diimide Zwitterionic Polymer for Photoacoustic Imaging Guided Photothermal/Photodynamic Synergistic Therapy with Single Near-Infrared Irradiation. *J. Mater. Chem. B.* **2018**, *6*, 3395-3403.

(35) Zhang, S.; Guo, W.; Wei, J.; Li, C.; Liang, X.; Yin, M. Terrylenediimide-Based Intrinsic Theranostic Nanomedicines with High Photothermal Conversion Efficiency for Photoacoustic Imaging-Guided Cancer Therapy. *ACS Nano* **2017**, *11*, 3797-3805.

(36) Liu, C.; Zhang, S.; Li, J.; Wei, J.; Müllen, K.; Yin, M. A Water-Soluble, NIR-Absorbing Quaterrylenediimide Chromophore for Photoacoustic Imaging and Efficient Photothermal Cancer Therapy. *Angew. Chem. Int. Ed.* **2019**, *58*, 1638-1642.

(37) Srinivas, M.; Melero, I.; Kaempgen, E.; Figdor, C. G.; de Vries, I. J. M. Cell Tracking Using Multimodal Imaging. *Contrast Media Mol. Imaging* **2013**, *8*, 432-438.

(38) Kircher, M. F.; Gambhir, S. S.; Grimm, J. Noninvasive Cell-Tracking Methods. *Nat. Rev. Clin. Oncol.* **2011**, *8*, 677-688.

(39) Wang, Y.; Xu, C.; Ow, H. Commercial Nanoparticles for Stem Cell Labeling and Tracking. *Theranostics* **2013**, *3*, 544-560.

(40) Ricles, L. M.; Nam, S. Y.; Treviño, E. A.; Emelianov, S. Y.; Suggs, L. J. A Dual Gold Nanoparticle System for Mesenchymal Stem Cell Tracking. *J. Mater. Chem. B* **2014**, *2*, 8220 – 8230.

(41) Dhada, K.; Hernandez, D. S.; Suggs, L. J. In Vivo Photoacoustic Tracking of Mesenchymal Stem Cell Viability. *ACS Nano* **2019**, *13*, 7791-7799.

(42) Yin, C.; Wen, G.; Liu, C.; Yang, B.; Lin, S.; Huang, J.; Zhao, P.; Wong, S. H. D.; Zhang, K.; Chen, X.; Li, G.; Jiang, X.; Huang, J.; Pu, K.; Wang, L. Organic Semiconducting Polymer Nanoparticles for Photoacoustic Labeling and Tracking of Stem Cells in the Second Near-Infrared Window. *ACS Nano* **2018**, *12*, 12201-12211.

(43) Kubelick, K. P.; Snider, E. J.; Ethier, C. R.; Emelizanov, S. Development of a Stem Cell Tracking Platform for Ophthalmic Applications Using Ultrasound and Photoacoustic Imaging. *Theranostics* **2019**, *9*, 3812-3824.

(44) Wais, U.; Chennamaneni, L. R.; Thoniyot, P.; Zhang, H.; Jackson, A. W. Main-Chain Degradable Star Polymers Comprised of pH-Responsive Hyperbranched Cores and Thermoresponsive Polyethylene Glycol-Based Coronas. *Polymer Chem.* **2018**, *9*, 4824-4839.

(45) Sengupta, S.; Dubey, R. K.; Hoek, R. W. M.; van Eeden, S. P. P.; Gunbaş, D. D.; Grozema, F. C.; Sudhölter, E. J. R.; Jager, W. F. Synthesis of Regioisomerically Pure 1,7-Dibromoperylene-3,4,9,10-tetracarboxylic Acid Derivatives. *J. Org. Chem.* **2014**, *79*, 6655-6662.

(46) Sukul, P. K.; Datta, A.; Malik, S. Light Harvesting and Amplification of Emission of Donor Perylene–Acceptor Perylene Aggregates in Aqueous Medium. *Chem.-Eur. J.* **2014**, *20*, 3019-3022.

(47) Gillich, T.; Acikgöz, C.; Isa, L.; Schlüter, A. D.; Spencer, N. D.; Textor, M. PEG-Stabilized Core–Shell Nanoparticles: Impact of Linear versus Dendritic Polymer Shell Architecture on Colloidal Properties and the Reversibility of Temperature-Induced Aggregation. *ACS Nano* **2013**, *7*, 316-329.

(48) Moore, T.L.; Rodriguez-Lorenzo, L.; Hirsch, V.; Balog, S.; Urban, D.; Jud, C.; Rothen-Rutishauser, B.; Lattuada, M.; Petri-Fink, A. Nanoparticle Colloidal Stability in Cell Culture Media and Impact on Cellular Interactions. *Chem. Soc. Rev.* **2015**, *44*, 6287-6305.

(49) Sharkey, J.; Lewis, P. J. S.; Barrow, M.; Salamah, M.A.; Noble, J.; Livingstone, E.; Lennen, R. J.; Jansen, M. A.; Carrion, J. G.; Liptrott, N.; Forbes, S.; Adams, D. J.; Chadwick, A. E.; Forbes, S. J.; Murray, P.; Rosseinsky, M. J.; Goldring, C. E.; Park, B. K.. Functionalized Superparamagnetic Iron Oxide Nanoparticles Provide Highly Efficient Iron-Labeling in Macrophages for Magnetic Resonance-Based Detection in Vivo. *Cytotherapy* **2017**, *19*, 555-569.

(50) Soenen, S. J. H.; De Guyper, M. Assessing Cytotoxicity of (Iron Oxide-Based) Nanoparticles: An Overview of Different Methods Exemplified with Cationic Magnetoliposomes. *Contrast Media Mol. Imaging* **2009**, *4*, 207-219.

(51) Riss, T. L.; Moravec, R. A.; Niles, A. L. ; Duellman, S. ; Benink, H. A. ; Worzella, T. J. ; Minor, L. Cell Viability Assays. [Updated 2016 July 1st]. In: Sittampalam, G.S.; Grossman, A.; Brimacombe, K. et al., Assay Guidance Manual (ed), Internet.

(52) Hwang, E.; Song, J.; Zhang, J. Integration of Nanomaterials and Bioluminescence Resonance Energy Transfer Techniques for Sensing Biomolecules. *Biosensors* **2019**, *9*, 42.

(53) Dragavon, J.; Blazquez, S.; Rekiki, A.; Samson, C.; Theodorou, I.; Rogers, K. L.; Tournebize, R.; Shorte, S. L. In Vivo Excitation of Nanoparticles Using Luminescent Bacteria. *PNAS* **2012**, *109*, 8890-8895.

(54) Juffroy, O.; Noël, D.; Delanoye, A.; Viltart, O.; Wolowczuk, I.; Verwaerde, C. Subcutaneous Graft Of D1 Mouse Mesenchymal Stem Cells Leads To The Formation Of A Bone-Like Structure. *Differentiation* **2009**, *78*, 223-231.

SYNOPSIS (ToC graph)